JGR Space Physics

RESEARCH ARTICLE
10.1029/2023JA031394

# Spatial Resolution in Inverse Problems: The EZIE Satellite Mission

**Michael Madelaire[1], Karl Laundal[1], Jesper Gjerloev[1,2], Spencer Hatch[1], Jone Reistad[1], Heikki Vanhamäki[3], Colin Waters[4], Anders Ohma[1], Rafael Mesquita[2], and Viacheslav Merkin[2]**

[1]Birkeland Centre for Space Science, University of Bergen, Bergen, Norway, [2]Johns Hopkins University Applied Physics Laboratory, Laural, MD, USA, [3]Space Physics and Astronomy Research Unit, University of Oulu, Oulu, Finland, [4]School of Mathematical and Physical Sciences, University of Newcastle, Callaghan, NSW, Australia

**Key Points:**

- A method for quantifying spatial resolution in inverse problems is presented
- We show that adding a ground magnetometer to a reconstruction based on Electrojet Zeeman Imaging Explorer satellite measurements improves accuracy locally and globally
- A method for reducing model complexity by combining regularization parameters is presented

**Correspondence to:**
M. Madelaire,
michael.madelaire@uib.no

**Citation:**
Madelaire, M., Laundal, K., Gjerloev, J., Hatch, S., Reistad, J., Vanhamäki, H., et al. (2023). Spatial resolution in inverse problems: The EZIE satellite mission. *Journal of Geophysical Research: Space Physics*, *128*, e2023JA031394. https://doi.org/10.1029/2023JA031394

Received 8 FEB 2023
Accepted 13 MAY 2023

The copyright line for this article was changed on 26 JUL 2023 after original online publication.



**Abstract** Inverse modeling has become one of the primary methods for studying ionospheric electrodynamics, especially when using magnetic field measurements from below the ionosphere. We present a method for quantifying the spatial resolution in an inverse model for non-uniformly sampled spatial data. This method provides a tool for assessing if a model can resolve the physical phenomena of interest. We quantify the spatial resolution for the Spherical Elementary Current System basis functions to model the ionospheric dynamics. Our results apply to models with spatially confined model parameters, unlike spherical harmonics where the model parameters describe the amplitude of global surface functions. The method is demonstrated for the upcoming Electrojet Zeeman Imaging Explorer cubesat mission which will provide spatially distributed remote sensing measurements of the magnetic field in the mesosphere. We show that, including measurements from a single ground magnetometer can significantly improve the spatial resolution. However, the impact of including a ground magnetometer depends on the relative position of the station with respect to the mesospheric measurements. In addition, a method for reducing two regularization parameters to one is presented. Reducing the amount of regularization parameters simplifies the optimization problem and facilitates a fair comparison between the models with and without a ground magnetometer.

## 1. Introduction

Historically, ground magnetometers have played a key role in the study of ionospheric electrodynamics (Amm et al., 2010) as observations of the ground magnetic perturbation allow for the determination of an equivalent horizontal ionospheric electrical current (Friis-Christensen et al., 1988). It is now common to use inverse modeling techniques to create regional and global estimates of such currents (Laundal et al., 2022; Madelaire et al., 2022; Richmond & Kamide, 1988). While the techniques used are very useful tools, it is sometimes forgotten that the resulting model depends on a series of choices made prior to solving the inverse problem. If these choices alter, then the conclusions drawn might change. It is therefore crucial that we, as a community, understand the limitations of our models to avoid drawing false conclusions and improve the methods with which we analyze data.

The solution to an inverse problem is inherently probabilistic. Regardless of the method, for example, least squares or a Monte-Carlo Markov-Chain algorithm, the solution is the most probable, that is, other solutions of similar probability are likely to exist. The distribution of these solutions is the posterior model distribution. Analyzing the spread of the posterior model distribution quantifies how prior information about the model and measurement uncertainties propagate into the solution, referred to as model variance. Furthermore, the underlying assumptions in the physical model can be a source of uncertainty. Juusola et al. (2020) showed how accounting for ground induced currents can impact the estimated ionospheric currents and their uncertainties. In addition to model variance, spatial resolution is an important attribute that can be addressed. It is determined by multiple factors:

1. The spatial distance between model parameters, assuming they are locally defined, unlike spherical harmonics where the model parameters describe global surface functions;
2. The spatial distance between observations and in the case of magnetic fields the distance between the measurement and source current;
3. The choice of regularization parameters.

Regarding the second factor, ground magnetometers are ~110 km from the ionospheric current responsible for the observed magnetic perturbation. As measurements are obtained from increasing distance from the source current its strength decreases, but this decrease is faster for small scale sizes resulting in a smoothing of the magnetic field with increasing distance (Laundal et al., 2021). This concept plays a large role in the spatial scales that can be resolved for example, by ground magnetometers. Regarding the third and perhaps least intuitive factor, it is common to perform zeroth order Tikhonov regularization or truncated singular value decomposition when an inverse problem is ill-posed. As the level of regularization increases the spatial resolution degrades. In other words, one should keep in mind when working with a regularized solution that the resulting spatial resolution will be affected by the choice of regularization parameter. The issue of choosing a regularization parameter can be addressed by using techniques such as the L-curve (Hansen, 1992). Bauer and Lukas (2011) provide a comprehensive comparison of different techniques. However, determining the right value of the regularization parameter is significantly more difficult when there is more than one.

Both model variance and spatial resolution are important attributes to evaluate. The former can be examined by determining the posterior model covariance (Cousins et al., 2015; Matsuo et al., 2015; Richmond & Kamide, 1988). Information about measurement uncertainty and prior information about the solution can be propagated through the inverse problem and provide the variance and covariance of the model parameters. The latter, to the knowledge of the authors, has not been explored in terms of the Spherical Elementary Current Technique (Spherical Elementary Current System [SECS]) (Amm & Viljanen, 1999). However, several studies have been reported from the tomography community (Gustavsson, 1998; Pascual-Marqui, 1999; Ren & Kalscheuer, 2020). Spatial resolution of a model parameter is often quantified by analyzing the spatial extent of its point-spread function (PSF). These functions are determined by the design of the inverse problem and can be analyzed without experimental data.

It is important to understand the spatial resolution with which a model can resolve structures. In one scenario, we may be looking for small scale structures in the model predictions to validate the existence of certain physical phenomena. A lack of such structures can only be considered significant if the model resolution implies that they should be detectable. It can be tempting to think of the spatial resolution purely as a function of the spatial distance between measurements, that is, the Nyquist sampling frequency. This would be applicable if a simple interpolation scheme was used on a series of measurements of a single magnetic field component. However, in an inversion scheme, for example, the SECS technique, the interpolation of the magnetic field is based on physics, that is, the existence of an equivalent current that can produce the observed magnetic field. Measurement uncertainty and the inclusion of prior information add to the complexity of the problem. The spatial resolution based on the Nyquist sampling frequency should therefore only be considered a lower limit.

As measurement techniques improve and provide increasingly spatial dense observations it becomes crucial to analyze the spatial resolution. Dense observations make it possible to resolve small scale features which provides opportunities to test hypotheses and perform new analyses. An example is the NASA satellite mission Electrojet Zeeman Imaging Explorer (EZIE) (Laundal et al., 2021; Yee et al., 2021) scheduled to launch late 2024 or early 2025. It will provide measurements of the magnetic field perturbation at mesospheric heights (~80 km). In order to answer the science questions posed by the mission, the reconstruction of the ionospheric horizontal electric current needs to be achieved on mesoscales (100–500 km).

In this study, we address the question of spatial resolution using EZIE as an example and introduce ground magnetometer measurements to understand how these additional data affect the model. We present a method for determining a relationship between the two regularization parameters controlling the zeroth and first-order Tikhonov regularization applied in this study. Combining the two parameters facilitates choosing suitable parameter values. Section 2 describes the design of our inverse problem an previous existing work on spatial resolution, and explains how we calculate spatial resolution. Section 3 presents the method used to combine and determine the two regularization parameters. Section 4 compares model predictions, spatial resolution, and model variance with and without the inclusion of a ground magnetometer. Sections 5 and 6 discusses the results and concludes the study, respectively.

## 2. Spatial Resolution

The term resolution refers to the accuracy with which something can be observed/measured (e.g., grid resolution, temporal/spatial resolution of measurements). The aim of this study is to quantify the accuracy with which the

spatial structure of the ionospheric current can be resolved that is, answering the question: What is the smallest spatial scale our model can resolve? We refer to this as *spatial resolution*.

### 2.1. The Inverse Problem

The EZIE satellite mission (Laundal et al., 2021; Yee et al., 2021) consists of three cubesats flying in a pearls-on-a-string formation and will image the magnetic structure of the ionosphere. Each satellite will have four sensors pointing toward Earth measuring oxygen thermal emissions in a push-broom configuration. The EZIE technique is based on the Zeeman splitting of the 118 GHz oxygen emission. The result of this technique is the ambient magnetic field in the mesosphere (Yee et al., 2017, 2021). This novel method of measuring the magnetic field results in an unprecedented spatial resolution close to the source current (~80 km altitude) compared to ground magnetometers (~0 km altitude).

Laundal et al. (2021) showed how the magnetic perturbation observed by an EZIE satellite could be used to retrieve an equivalent ionospheric electric current using the SECS technique (Amm & Viljanen, 1999; Amm et al., 2002). The synthetic data used by Laundal et al. (2021) were based on the Gamera (MHD) model (Sorathia et al., 2020; Zhang et al., 2019). Magnetic field perturbations were determined using the Magnetosphere-Ionosphere Coupler/Solver code (Merkin & Lyon, 2010) rewritten for Gamera. The magnetic field perturbations are used together with a main field model and an atmospheric model to simulate mesospheric $O_2$ microwave emissions. A realistic model of the EZIE instrument performance (including various noise sources and uncertainties) was then used, together with the emissions, to generate realistic measurements. Finally, an inversion, explained in detail by Yee et al. (2021), was computed to retrieve simulated magnetic field measurements with realistic noise. Since that paper was published the viewing angle of the four sensors has been changed resulting in a new synthetic data set that will be used here. This new data set was produced in the same way as before and contains 3D vector magnetic field perturbations, along the satellite's four tracks. The measurements are provided with 3-s cadence in agreement with the EZIE integration time. Furthermore, the variance of each component along with the covariance between the three vector components is included.

Figure 1 is a snapshot of the radial magnetic field perturbation ($\Delta B_r$) in the northern polar hemisphere from the MHD simulation used to generate the synthetic data set. The dotted lines represent the four tracks along which the satellite's four sensors measure the magnetic field. The black square is the boundary of the grid used in the inverse problem and the solid blue/orange/green/red lines, inside the black square, indicate the part of the satellite trajectory used in the inversion. The grid has been extended beyond the region where data are provided for illustration purposes. Model predictions outside the region of data are subject to extrapolation. It is outside the scope of this study to determine how far it is safe to extrapolate.

The forward problem can be written as

$$\boldsymbol{d} = \boldsymbol{G}\boldsymbol{m}, \tag{1}$$

where $\boldsymbol{d}$ is a column vector with measurements of the magnetic field components ($\Delta B_r$, $\Delta B_\theta$, $\Delta B_\phi$), $\boldsymbol{m}$ is a column vector with model parameters that scale the strength of the divergence-free current field around each SECS pole and $\boldsymbol{G}$ is a matrix containing the linear relationship between $\boldsymbol{d}$ and $\boldsymbol{m}$, often referred to as the design matrix. An estimate of $\boldsymbol{m}$ can be written in terms of a regularized least squares solution (Aster et al., 2013; Neumaier, 1998; Tikhonov & Arsenin, 1977)

$$\begin{aligned} \tilde{\boldsymbol{m}} &= \boldsymbol{G}^{\dagger}\boldsymbol{d} = \left(\boldsymbol{G}^T\boldsymbol{C}_d^{-1}\boldsymbol{G} + \boldsymbol{C}_m^{-1}\right)^{-1}\boldsymbol{G}^T\boldsymbol{C}_d^{-1}\boldsymbol{d} \\ \boldsymbol{C}_m^{-1} &= \lambda_1\boldsymbol{I} + \lambda_2\boldsymbol{L}^T\boldsymbol{L}. \end{aligned} \tag{2}$$

The column vector $\boldsymbol{m}$ is the true model while $\tilde{\boldsymbol{m}}$ is the estimated model. Here $\boldsymbol{G}^{\dagger}$ is the generalized inverse of $\boldsymbol{G}$, $\boldsymbol{C}_d$ is the data covariance matrix, and $\boldsymbol{C}_m$ is the prior model covariance matrix. This inverse problem is ill-posed due to the spatial distribution of measurements and the amount of measurements compared to model parameters. Therefore, regularization is required to stabilize the solution. We employ a regularization scheme similar to Laundal et al. (2021); $\lambda_1\boldsymbol{I}$ minimizes the 2-norm of the model while $\lambda_2\boldsymbol{L}^T\boldsymbol{L}$ smooths the gradients of the SECS amplitudes in the magnetic east/west direction. Both $\lambda_1$ and $\lambda_2$ are regularization parameters to be determined, $\boldsymbol{I}$ is the identity matrix, and $\boldsymbol{L}$ describes the finite difference calculation of east/west gradients. The stability of

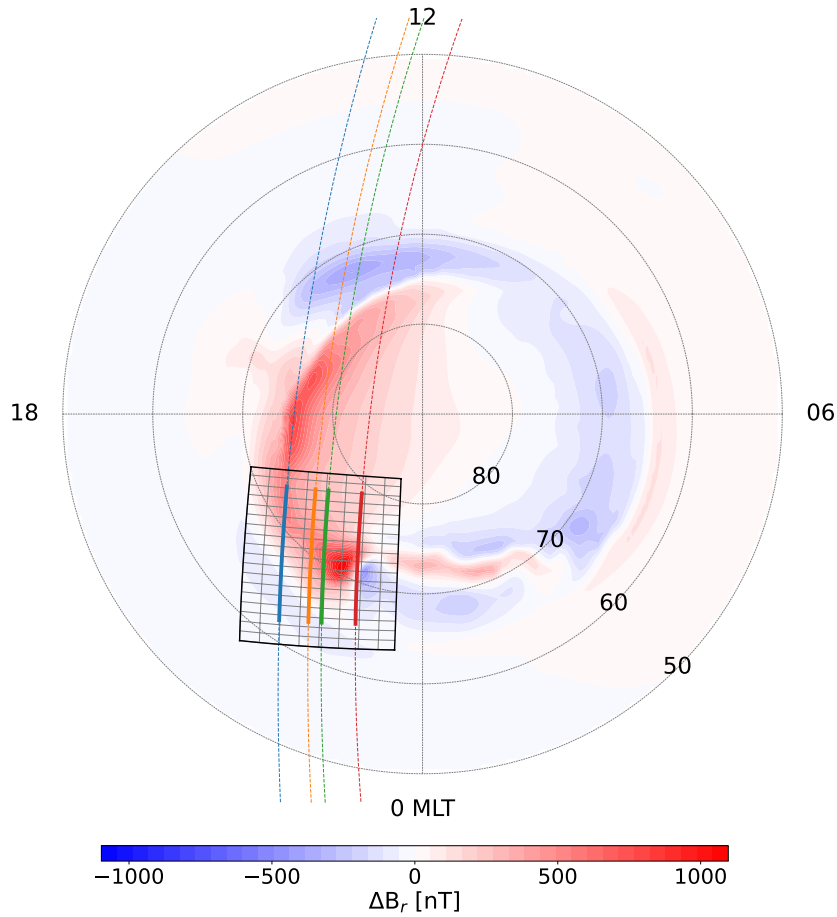


**Figure 1.** Illustration of $\Delta B_r$ (80 km altitude) in the northern polar hemisphere from an MHD simulation (Gamera (Sorathia et al., 2020; Zhang et al., 2019)). A crossing by one of the Electrojet Zeeman Imaging Explorer satellites is overlain and the foot points (80 km altitude) of its four sensors are indicated by the dotted lines. The black square is the boundary of the grid used in the inverse problem to reconstruct the equivalent ionospheric horizontal electric current. The gray grid is a coarse version of the cubed sphere grid on which the model is defined (Laundal et al., 2021). The solid colored lines show where the data used in our inverse problem is located. The point of the figure is to give an overview of the geometry of the inverse problem before we zoom in on the black square.

the model is challenged by the spatial separation between the four measurement tracks. The east/west gradient smoothing is included to stabilize the model between the tracks by assuming that current structures typically are aligned east/west. However, the solution is still data driven as there is no hard boundary on the possible gradients.

The variance of the model parameters and the covariance, as a result of measurement uncertainty and $\boldsymbol{C}_m$, is contained in the posterior model covariance matrix (Aster et al., 2013)

$$\boldsymbol{C}_{pm} = \left(\boldsymbol{G}^T \boldsymbol{C}_d^{-1} \boldsymbol{G} + \boldsymbol{C}_m^{-1}\right)^{-1}. \tag{3}$$

It is important to recognize that this is not an uncertainty related to how well the model reproduces the truth, but an uncertainty in the model parameters based on the information provided. As such, the posterior model covariance will decrease as the importance of regularization is increased. The uncertainty described by $\boldsymbol{C}_{pm}$ can be projected into any other quantity of interest, as long as there exists a linear relationship with the model. The posterior data covariance matrix can be written as

$$\boldsymbol{C}_{pd} = \boldsymbol{A}\boldsymbol{C}_{pm}\boldsymbol{A}^T, \tag{4}$$

which can be used to examine how variance in the model is reflected in predictions of the magnetic field.

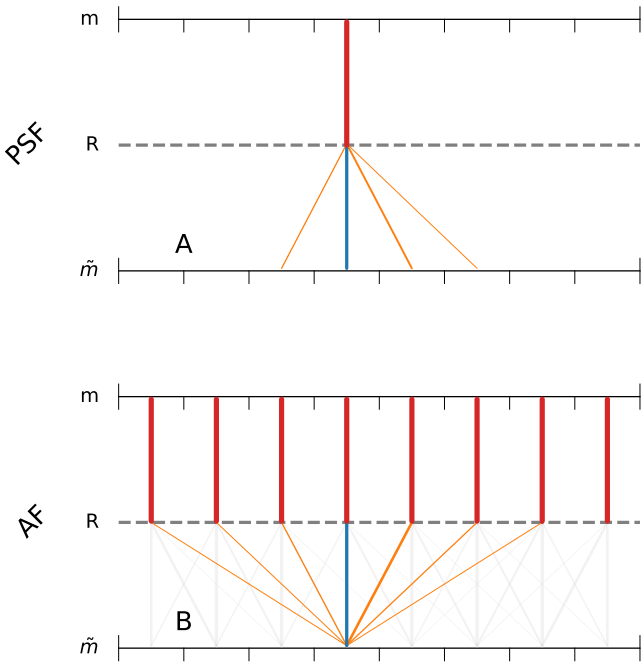


**Figure 2.** A conceptual illustration of averaging functions (AFs) and point-spread functions (PSFs). Imagine $\boldsymbol{R}$ to be a filter through which light passes. $\boldsymbol{m}$ is the light source and $\tilde{\boldsymbol{m}}$ is the observed pattern after the light passes through $\boldsymbol{R}$. Panel (a)illustrates how light from a single point source spreads after passing through $\boldsymbol{R}$, that is, a PSF. Panel (b) illustrates how the light observed at one location is a linear combination of multiple point sources, that is, an AF. The point of this figure is to provide a conceptual idea of AFs and PSFs before and after we introduce 2D versions and discuss how to derive information from them.

### 2.2. Quantifying Spatial Resolution

The subject of spatial resolution has been explored extensively in the tomography community; magnetotellurics, seismology, electroencephalograms, etc. (Gustavsson, 1998; Pascual-Marqui, 1999; Ren & Kalscheuer, 2020). Although the scientific topics vary from medicine to geophysics, the underlying inverse problem is often similar. In tomography, the model parameters, for example, conductivity, tend to be the quantity of interest. If a $5 \times 5$ grid is used then there are 25 unknown conductivity values. In our inverse problem, the model parameters are similarly defined on a grid and represent the amplitude of the divergence-free current associated with the individual SECS poles. Therefore, the methods for quantifying spatial resolution in tomography are applicable here. In this study, spatial resolution refers to the ability of the inverse problem to resolve a model parameter, that is, the strength of the divergence-free current in a single cell of the model grid.

The true model, $\boldsymbol{m}$, can be directly related to the estimated model, $\tilde{\boldsymbol{m}}$, by combining Equations 1 and 2

$$\tilde{\boldsymbol{m}} = \boldsymbol{G}^{\dagger}\boldsymbol{G}\boldsymbol{m} = \boldsymbol{R}\boldsymbol{m}. \tag{5}$$

The model resolution matrix, $\boldsymbol{R}$, describes how well the model parameters are resolved in the estimated model. If $\boldsymbol{R}$ is the identity matrix $\tilde{\boldsymbol{m}}$ is perfectly resolved, that is, $\tilde{\boldsymbol{m}} = \boldsymbol{m}$. However, for regularized solutions, it is more common that $\boldsymbol{R}$ contains non-zero off-diagonal elements suggesting that the model parameters are not perfectly resolved. The level to which the individual model parameters are resolved can be determined by examining the rows and columns of $\boldsymbol{R}$. The rows are referred to as averaging functions (AFs) and columns as PSFs. Miller and Routh (2007), Oldenborger and Routh (2009), and Ren and Kalscheuer (2020) provide an overview of these concepts. Here we attempt to give a conceptual illustration of AFs and PSFs by viewing $\boldsymbol{R}$ as a filter through which light passes. Figure 2a illustrates how a single point source is spread out as it passes through $\boldsymbol{R}$. This is a PSF and is equivalent to evaluating Equation 5 when $\boldsymbol{m}$ is a $\delta$-function. Figure 2b shows how a single value of $\tilde{\boldsymbol{m}}$ is a linear combination of multiple point sources. This linear combination is the AF and is important for understanding the interpolation between different spatial locations.

Various approaches for quantifying spatial resolution have previously been presented. Tarantola and Valette (1982) suggested using the posterior model covariance matrix, Barmin et al. (2001), An (2012), and Chiao et al. (2014) suggested using AFs, and Miller and Routh (2007) and Oldenborger and Routh (2009) suggested using PSFs. However, as pointed out by Oldenborger and Routh (2009), several studies, including some cited here, confuse the terms AF and PSF. This is understandable as the AFs and PSFs can be identical if the inverse problem is not regularized or if truncated SVD was used (Oldenborger & Routh, 2009). Miller and Routh (2007) studied the resolving capabilities of AFs and PSFs and concluded that PSFs were better suited for determining spatial resolution. For this reason, we use the PSF when quantifying spatial resolution.

Figure 3 shows the absolute PSF for the model parameter located at the cyan dot on a map similar to Figure 1. Contrary to the conceptual illustration of a PSF in Figure 2, the PSFs are not limited to positive values as the model parameters can be negative. We therefore take the absolute value of the PSF before quantifying the spatial resolution. The figure also illustrates how PSFs are elongated in the east/west direction when constraints are placed on the smoothness of the east/west gradients. On the bottom and to the right of the map we show the projection of the PSF onto one axis. The projection is the sum over the PSF in a specific direction and can be thought of as a marginal distribution. In addition, Figure 3 summarizes the result of three methods for quantifying spatial resolution. Barmin et al. (2001) and An (2012) suggested quantifying the spread by fitting an appropriate function to the PSF. Two ellipses indicating a non-linear fit of a 2D Gaussian function. The innermost is the Full Width Half Maximum (FWHM) ($2.335\sigma$) while the outermost is $\pm 3\sigma$, where $\sigma$ is the standard deviation of the fitted Gaussian distribution. The FWHM of the marginal distributions is shown as an orange shaded area overlain the

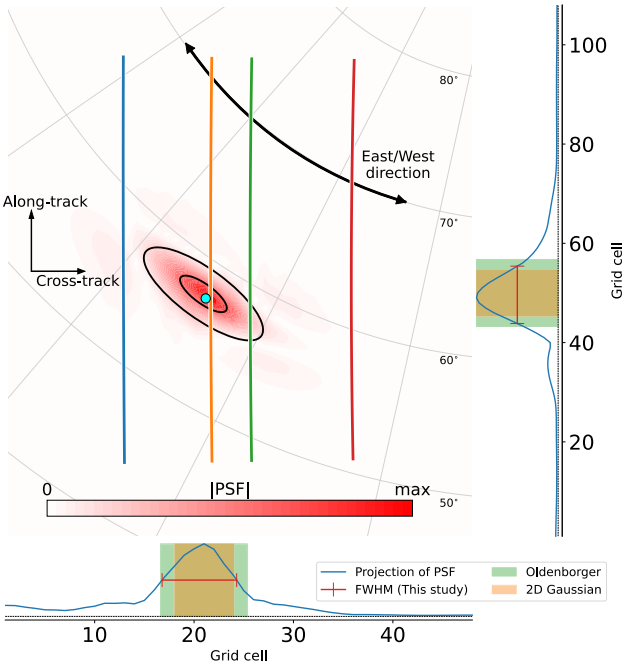


**Figure 3.** Illustration of a point-spread function (PSF) and a comparison of three ways to quantify spatial resolution. The map is a close-up of the black square in Figure 1 and the contour is the absolute of the PSF associated with the model parameter located at the cyan dot. The four colored vertical lines indicate the foot points of the satellite's four sensors and the black ellipses represent a non-linear fit of a 2D Gaussian function. The graphs on the bottom and the right-hand side are projections of the PSF. The green shaded area reflects the result of using the spread metric suggested by Oldenborger and Routh (2009), under the assumption that the PSF is Gaussian. The orange shaded area is the Full Width Half Maximum (FWHM) of the marginal distribution of the 2D Gaussian fit. The red line is the FWHM of the projection of the PSF which we use to quantify spatial resolution. The point of this figure is to help visualize a PSF and provide a platform on which methods for quantifying spatial resolution can be compared.

projected PSF. The FWHM is the minimum distance between two impulses for them to be distinguished from each other. This method is informative as it provides the rotation of the PSF. The downside is its complexity as it requires a non-linear fit which when automated can result in substantial errors.

Oldenborger and Routh (2009) presented a spread metric, similar to Miller and Routh (2007), based on the definition of variance using the squared PSF as a probability mass function. To translate the spread metric into the FWHM one must assume some known distribution. We assumed the PSF to be Gaussian, requiring a scaling of the spread metric by $\sqrt{2}$, the result is illustrated as a green-shaded area. We quantify spatial resolution as the FWHM of the projected PSF, shown on the axis of Figure 3. This is done by locating the first point, on either side of the maximum, to fall below 50% of the maximum. Linear interpolation between the point above and below 50% of the maximum is used to estimate the FWHM. The results are shown as red lines spanning the projected PSF. The spatial resolution estimates are provided in the cross- and along-track directions as these reflect the geometry of the EZIE measurements.

## 3. Combining Regularization Parameters

We are interested in quantifying spatial resolution to better understand the performance of a model. Similarly, we are interested in how combining measurements from different sources affects spatial resolution, for example, EZIE and ground magnetometer measurements. When comparing the resolution of two models it is crucial that the regularization parameters are determined objectively. It is tempting to tune them manually until the model predictions look "right," but these parameters have a direct impact on the spatial resolution and model variance and should be chosen with care. If not, one might under- or over-regularize resulting in a scenario where the results are not reproducible since values were chosen subjectively. This is where methods such as the L-curve (Hansen, 1992) come into play. The L-curve allows a trade-off between minimizing the data misfit and the part of the cost function controlled by the regularization. However, the L-curve is commonly applied to problems with a single regularization parameter and we have two. Therefore, we present an approach to determine a relationship between $\lambda_1$ and $\lambda_2$, referred to as the $\lambda$-relation, allowing the use of the L-curve for a single regularization parameter.

The $\lambda$-relation is based on $\boldsymbol{R}$. The AFs (rows of $\boldsymbol{R}$) describe the linear relationship between $\tilde{\boldsymbol{m}}$ and $\boldsymbol{m}$. The AF of a model parameter spatially close to a measurement will be sparse as that model parameter only will depend on other model parameters close to itself. The AF of a model parameter far away from measurements will depend on a much larger group of model parameters as those close to it also are poorly constrained by data. When the east/west gradients are smoothed, controlled by $\lambda_2$, the model parameters between the measurements, for example, the green and red data track, will become less dependent on the model parameters in their immediate vicinity and more dependent on those close to measurements. In other words, for moderate values of $\lambda_2$ the AF between the data tracks becomes more sparse. If the gradient smoothing is increased the dependence will not only be on the model parameters around the nearest measurements but also on those close to measurements on other data tracks (following a path of equal latitude). At this point, the AF becomes less sparse. We find that the models perform best when the model parameters between data tracks mainly depend on the nearest measurements. Achieving this coincides with the sparsest AF, that is, the linear relationship that depends on the least amount of other model parameters.

Figure 4 is a conceptual illustration of how we determine the $\lambda$-relation. Figure 4a is a map of the Hoyer index (Hoyer, 2004) over the AFs for a specific $\lambda_1$ and $\lambda_2$. The Hoyer index,

$$\text{information} = \frac{\sqrt{n} - \frac{\|\text{AF}\|_1}{\|\text{AF}\|_2}}{\sqrt{n} - 1}, \tag{6}$$

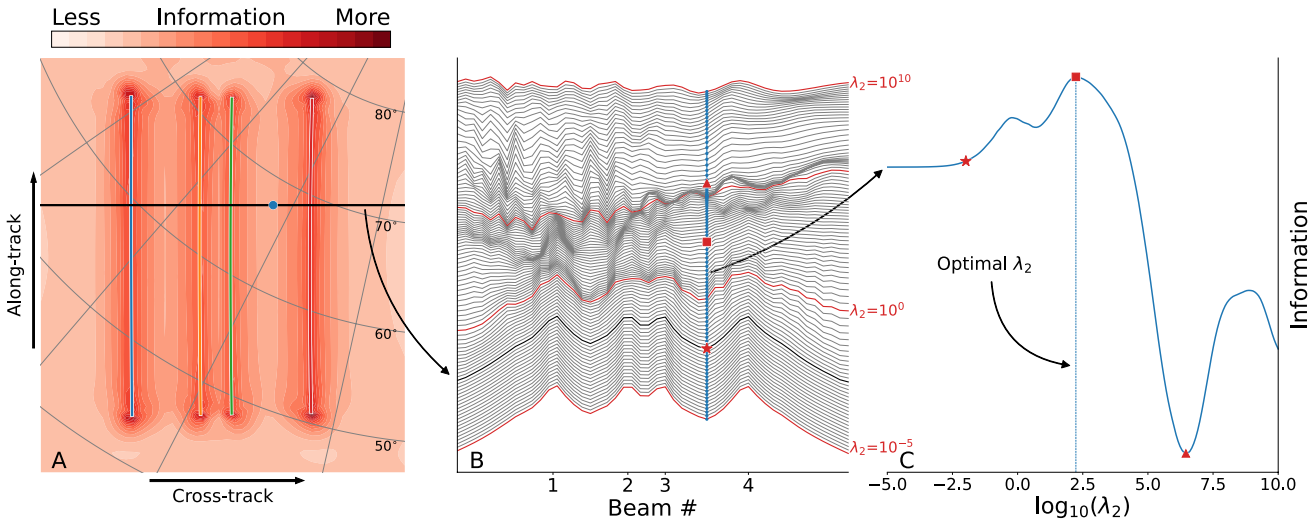


**Figure 4.** Conceptual illustration of how the $\lambda$-relation is determined. Panel (a) shows the Hoyer index of the averaging functions for a specific $\lambda_1$ and $\lambda_2$. Panel (b) shows how the cross-section in panel (a) changes with $\lambda_2$, while keeping $\lambda_1$ constant. Panel (c) shows how the Hoyer index changes as a function of $\lambda_2$ for the model parameters furthest away from data. The point of this figure is to provide a conceptual idea of how the "optimal" $\lambda_2$ is determined for a given $\lambda_1$.

is the normalized ratio of the 1- and 2-norm making it well suited for quantifying information/sparsity/entropy (Hurley & Rickard, 2008). Here $n$ is the size of the AF (the number of model parameters). Areas with high information reflect sparse AFs while areas with low information reflect denser AFs. Figure 4b shows a movie of how a cross-section of the map in Figure 4a changes if $\lambda_1$ is kept constant and $\lambda_2$ is varied. When $\lambda_2$ is small, that is, little to no gradient smoothing, there is a big difference between the information contained in the AFs close to and further away from measurements. However, as $\lambda_2$ increases the relative difference between the information contained in the AFs decreases. We are specifically interested in how information in the AF belonging to the model parameter furthest away from data changes as a function of $\lambda_2$. This model parameter is located halfway between the green and red track and its position on the cross-section is illustrated by a blue dot and line in Figures 4a and 4b, respectively. Figure 4c shows how the information in that AF changes as a function of $\lambda_2$. Initially, when $\lambda_2$ increases there is little to no change. At around $\log_{10}(\lambda_2) = -2$ (red star) the information starts to increase. Then, around $\log_{10}(\lambda_2) = 2.5$ (red square) the information is maximized and starts to decrease. This means that for the specific $\lambda_1$ used to create Figure 4 we have found the $\lambda_2$ that maximizes the information used to determine the model parameter furthest away from measurements.

By repeating the process summarized in Figure 4 for a series of $\lambda_1$ values a $\lambda$-relation can be generated as illustrated in Figure 5. For each value of $\lambda_1$ the $\lambda_2$ value that maximizes information is selected. In addition, we select the surrounding nine $\lambda_2$ that have the next highest information. This is done to help provide the B-spline fit, used to make the $\lambda$-relation continuous, information about the gradient. The $\lambda$-relation is shown for both cases explored in Section 5, that is, with and without a ground magnetometer.

It is now possible to solve the inverse problem repeatedly while changing $\lambda_1$, using the $\lambda$-relation to determine $\lambda_2$, to create an L-curve from which the "optimal" pair of $\lambda_1$ and $\lambda_2$ can be determined. The L-curve does have some difficulties. The best trade-off is found in the "knee." There have been many suggestions on how to determine this point, some of which are discussed by Hansen et al. (2007). We use the Kneedle algorithm (Satopaa et al., 2011), via. the python implementation (Arvai, 2020), that is designed to find the point of largest curvature. Figure 6 shows the L-curve. The knee has been marked by a black dot from which $\lambda_1$ and $\lambda_2$ can be determined. These are the $\lambda_1$ and $\lambda_2$ values used to create the models examined in Section 5.

## 4. Results

In this section, we compare model predictions, spatial resolution, and model variance when solving the inverse problem with synthetic measurements from EZIE with and without a single ground magnetometer. The ground magnetometer was included by adding two 3D vector measurements assuming a 1-min cadence, which

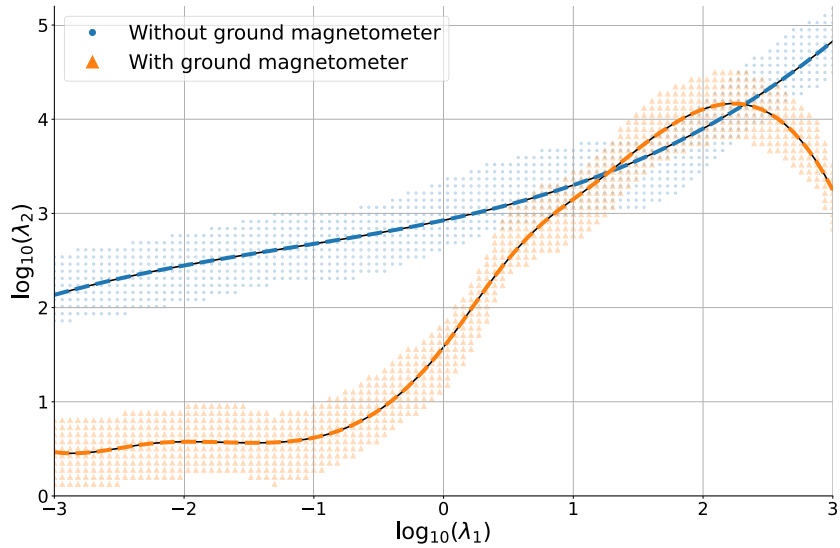


**Figure 5.** The $\lambda$-relations for the two models using Electrojet Zeeman Imaging Explorer data with (orange) and without (blue) an additional ground magnetometer. The dots show the 10 $\lambda_2$ that result in the highest Hoyer index for each $\lambda_1$. The dashed lines are B-spline fits to make the $\lambda$-relation continuous. The purpose of this figure is to explain how we go from the figure to a continuous $\lambda$-relation.

approximately corresponds to the temporal span of the EZIE measurements used. The two ground magnetometer measurements are taken directly from the MHD simulation, thus reflecting the truth. Their uncertainty is assumed to be 1 nT, which is 2–3 orders of magnitude lower than the EZIE measurements.

EZIE and ground magnetometers both provide measurements below the ionosphere, which means they are only affected by the divergence-free part of the ionospheric electric current. Therefore, these measurements are easily combined in an inversion. Figure 7 compares the truth (MHD, first column), to the predictions from two models: one based only on EZIE measurements (second column), and one that also includes a single ground magnetometer (third column). Each row refers to one of the magnetic field components ($\Delta B_r$, $\Delta B_\theta$, and $\Delta B_\phi$). The gray arrows illustrate the divergence-free ionospheric electric current, from the MHD, responsible for the magnetic

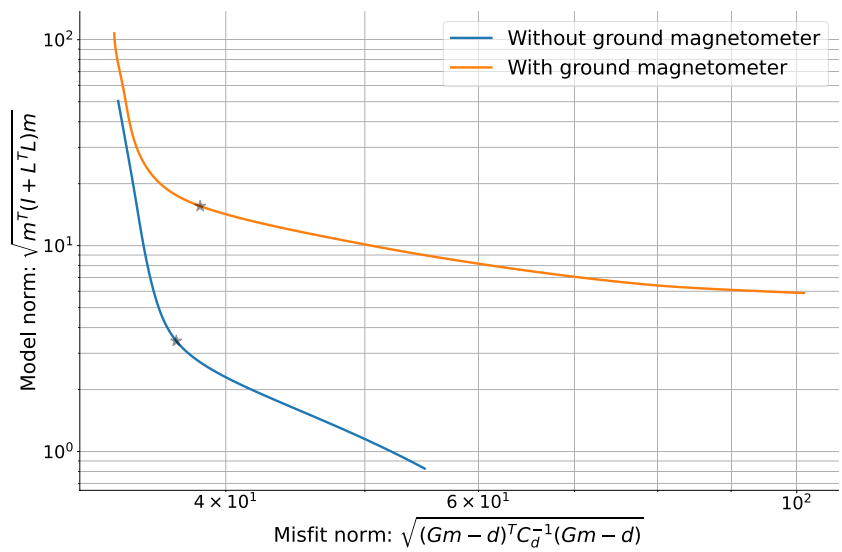


**Figure 6.** L-curve for the two models after testing numerous pairs of $\lambda_1$ and $\lambda_2$. The black dot indicates the best trade-off and was determined using the Kneedle algorithm (Satopaa et al., 2011). The point of this figure is to show how both regularization parameters are easily determined using the classic L-curve after having determined the $\lambda$-relation.

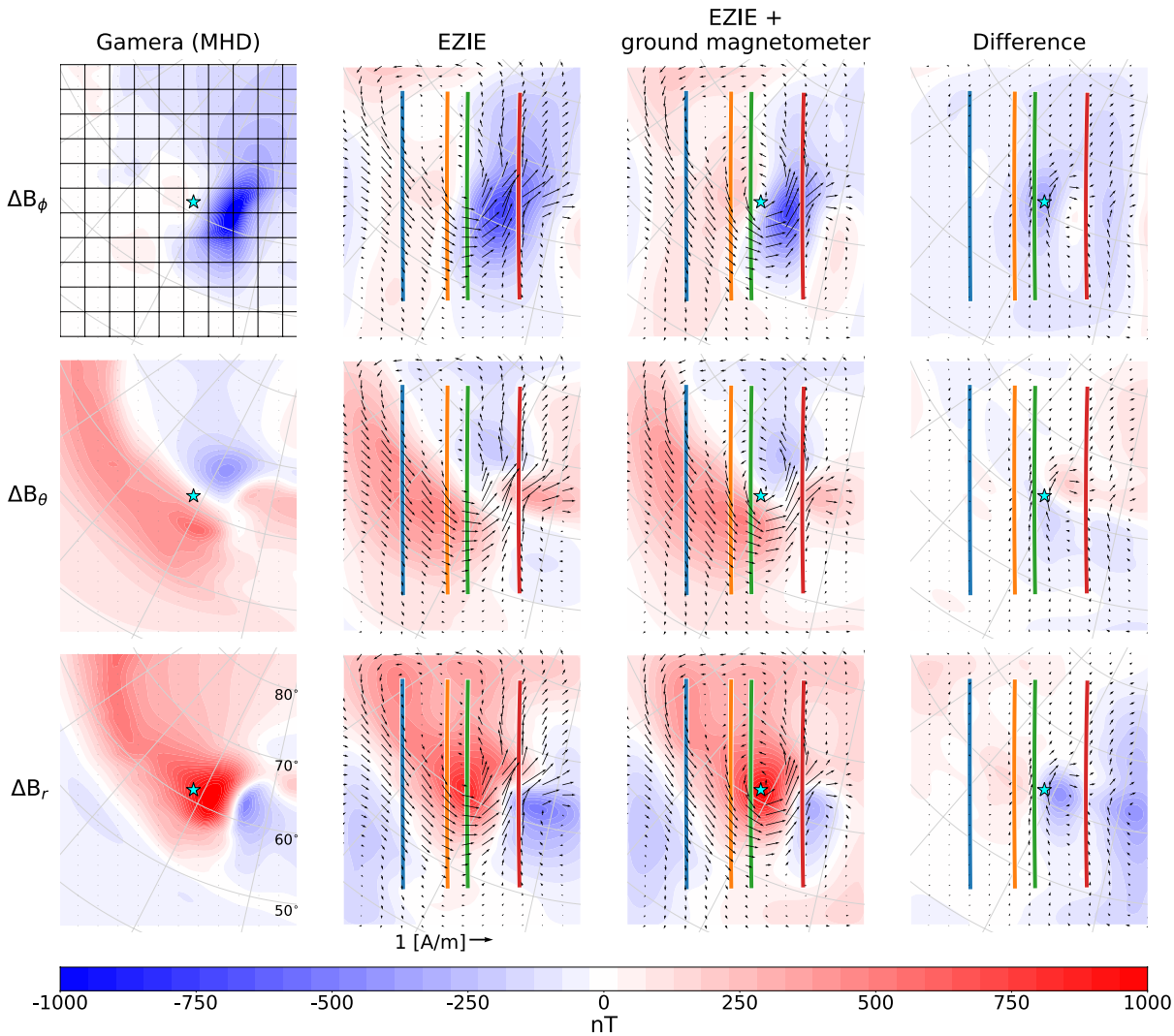


**Figure 7.** Comparison of the truth (MHD), first column, the model predictions based on Electrojet Zeeman Imaging Explorer measurements, second column, and model predictions after including the ground magnetometer, third column. The difference between the two models is shown in the fourth column, calculated by subtracting the third column from the second. The ground magnetometer's location is marked by a star. Each row shows a contour of one of the three magnetic field components $(\Delta B_\phi, \Delta B_\theta, \Delta B_r)$. The gray arrows show the divergence-free current from the MHD, while the black arrows show the equivalent ionospheric current determined from the models. The point of this figure is to show how well the models reproduce the truth.

perturbation below the ionosphere while the black arrows illustrate the equivalent ionospheric electric current as produced by the models. The four vertical lines (blue/orange/green/red) indicate the location of the EZIE measurements at 80 km altitude while the cyan star marks the location of the ground magnetometer.

Both the magnetic perturbation and ionospheric current are reconstructed rather well by both models. Outside the regions of data, the models perform worse which is no surprise as they are simply extrapolating. Between the green and red data tracks the MHD shows a current vortex that is better resolved in the model that includes a ground magnetometer. The difference between the two models is shown in the fourth column of Figure 7, calculated by subtracting the third column from the second. The difference is most prominent near the ground magnetometer. However, such qualitative comparisons do not provide details of the inherent properties of the models. Quantifying spatial resolution and model variance can provide an idea of how trustworthy the features in Figure 7 are and what physical phenomena can be resolved.

The first column of Figure 8 shows the spatial resolution in the cross- and along-track directions for the model based only on EZIE measurements, calculated as described in Section 2.2. The black background is visible when

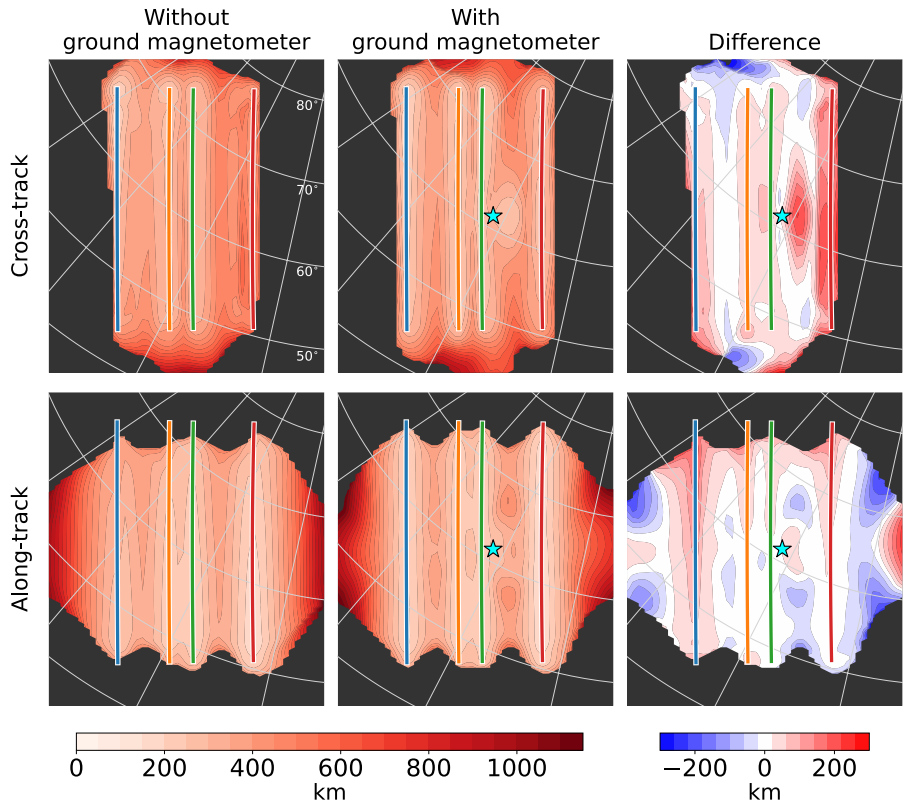


**Figure 8.** Comparison of the spatial resolutions in both cross- and along-track directions before and after including a single ground magnetometer. The difference, in the third column, is calculated by subtracting the second column from the first. A positive value thus means that the spatial resolution improved after including the ground magnetometer. The point of this figure is to show how a single measurement with low uncertainty, for example, from a ground magnetometer, can lead to significant improvements in the spatial resolution.

the FWHM could not be determined. This occurs when it is not possible to find a point smaller than 50% of the maximum on either side of the maximum. We see that the cross-track resolution is around 200–400 km with the lowest values close to the data and the highest values located between tracks. Looking at the along-track resolution we find that it is slightly lower, around 100–300 km. The areas where the FWHM could not be determined change depending on the direction of the spatial resolution. We suggest only considering the spatial resolution determined at locations constrained by more than one data point. That is, any value outside the blue and red track should be ignored, as well as values too close to the beginning and end of the data tracks. The second column in Figure 8 shows the spatial resolution after introducing the ground magnetometer while the third column shows the difference. The second column was subtracted from the first which means that a positive value indicates that the resolution has improved after including the ground magnetometer.

The spatial resolution in the cross-track direction between the ground magnetometer and the red track has improved by up to ∼200 km. Oddly, little to no improvement is seen between the ground magnetometer and the green/orange track which could be an indication of the minimum scale size that a ground magnetometer can resolve due to its distance to the ionosphere. The spatial resolution in the along-track direction did not significantly change. However, symmetrically above and below the ground magnetometer, in the along-track direction, the spatial resolution degraded slightly. We attribute this to the elongation of the PSF toward the ground magnetometer due to its low measurement uncertainty. Additionally, the inclusion of the ground magnetometer has an indirect global impact on the spatial resolution. By including the ground magnetometer the amount of east/west gradient smoothing necessary to stabilize the model has decreased. As a result the PSFs become more circular. This deformation occurs in east/west and north/south which maps into the cross- and along-track directions differently depending on location. The changes in spatial resolution due to the deformation of the PSFs is most pronounced in the along-track direction close to the data tracks. The improvements in spatial resolution after inclusion of the

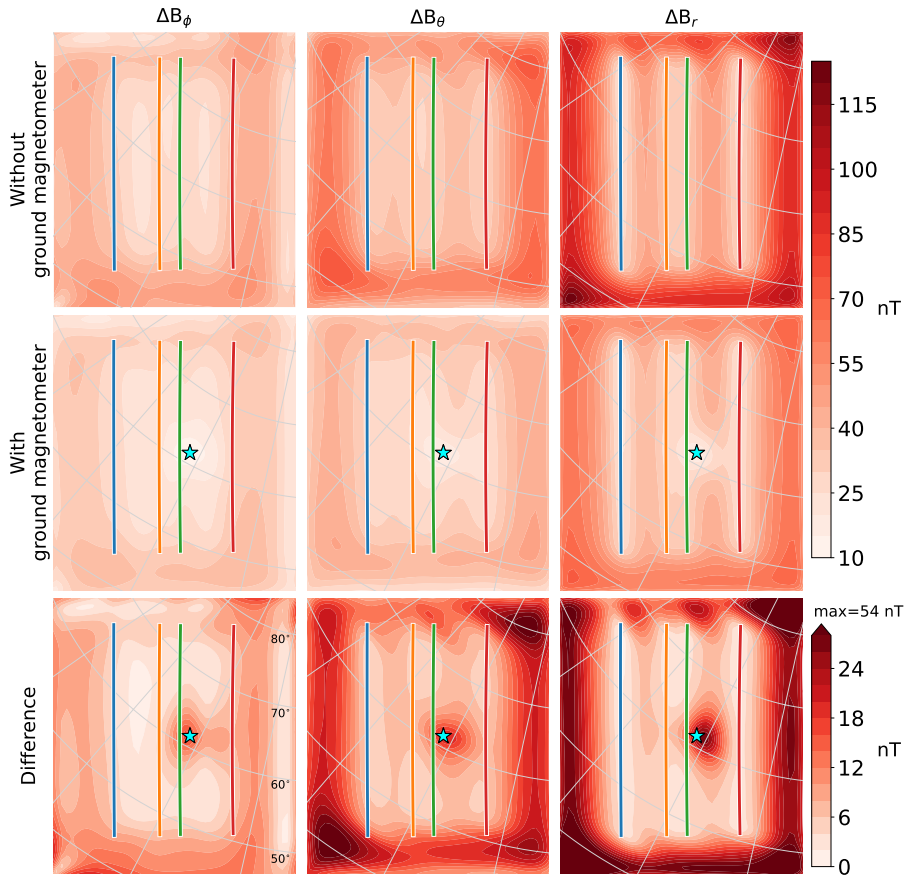


**Figure 9.** Comparison of the posterior data variance before and after including the ground magnetometer. The third row shows the difference between the first two rows, calculated by subtracting the second row from the first. The point is to show that even though the ground magnetometer mainly impacted the spatial resolution locally it affected the posterior data covariance both locally and globally.

ground magnetometer depends on the location and noise level of the ground magnetometer as well as the noise level and spatial separation between the EZIE measurements. It is therefore not possible to provide a single quantity to summarize the expected improvement when including ground magnetometer measurements.

Although the spatial resolution becomes worse in some areas after introducing the ground magnetometer, one should not conclude that the ground magnetometers have a negative impact on the model. This is clear when examining the posterior data covariance matrix, $\boldsymbol{C}_{pd}$. In Figure 9 the square root of the diagonal of $\boldsymbol{C}_{pd}$ is visualized when $\boldsymbol{A}$ (Equation 4) is the linear relationship between the model and the individual magnetic field components. The columns are ordered as $\Delta B_\phi$, $\Delta B_\theta$, and $\Delta B_r$ while the first two rows refer to the model with and without a ground magnetometer, respectively. Furthermore, the third row shows the difference between the models, calculated by subtracting the second row from the first. This implies that positive values are improvements due to the inclusion of the ground magnetometer. There are two clear differences. First, the variance decreases on a global level as the ground magnetometer measurements provide the model with additional information about the magnitude of the magnetic perturbation. Second, the variance is decreased in the area immediately around the ground magnetometer.

We did not find any substantial differences from the comparison of model predictions in Figure 7, except close to the current vortex after the introduction of the ground magnetometer. However, Figure 8 showed a clear improvement in spatial resolution. Figure 9 showed how the variance in the model prediction was reduced, both globally and locally. It should therefore be clear that examining attributes such as spatial resolution and model variance should be a more common practice as they contain crucial information regarding the design of the inverse problem and the performance of its solution.

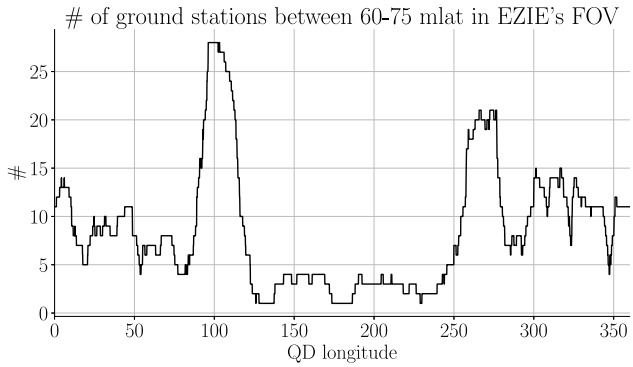


**Figure 10.** The estimated number of ground magnetometers in the Electrojet Zeeman Imaging Explorer field of view. This is based on the ground magnetometers available at SuperMag. The point of this figure is to show that the improvements, after including the ground magnetometer, shown in our study will be possible to achieve in every orbit and likely be better as many ground magnetometers will be available (the median is 7).

## 5. Discussion

In this study, we presented a method for quantifying spatial resolution when modeling ionospheric dynamics with SECS. Our method quantifies the spatial resolution of the model parameters, that is, the strength of the divergence-free current, by assessing the width of PSFs. This type of approach is called a resolution test (Aster et al., 2013). In general, the resolution test involves testing how the true model, $\boldsymbol{m}$, changes when passed through $\boldsymbol{R}$. The most common approach is to use a spike model, which we refer to as a $\delta$-function, where only one model parameter is non-zero (Rawlinson & Spakman, 2016). Using a $\delta$-function is in reality a special case. It would likewise be informative to test true models with different shapes, sizes, and/or gradients. However, it is not feasible to test all possible scenarios and we therefore only show resolution tests with the $\delta$-function. In addition to the strength of the divergence-free current, we are also interested in the horizontal current and associated magnetic field that can be derived from the model parameters. The magnetic field has three components and the horizontal current two, totaling five quantities. To avoid confusion over six different spatial resolutions we have chosen to work specifically with those related directly to the model parameters. It is possible to examine the spatial resolution of the other quantities. However, this requires formulation of a structure, for example, in $\Delta B_r$, in terms of a true model that can be passed through $\boldsymbol{R}$. The resulting model can be used to calculate model predictions that can be compared with the truth. The only issue is how to get the true model. One way, in case of synthetic data, could be to solve the inverse problem with a very high and even data coverage, along with no measurement noise. This would likely make the inverse problem well-posed and thus require virtually no regularization. The resulting model could be considered the truth.

It is tempting to think that an alternative to examining $\boldsymbol{R}$ is to test how well a model can reproduce a checkerboard pattern. The size of the tiles could be varied to find the smallest resolvable size. Although the method is intuitive and illustrative, Lévěque et al. (1993) showed it to be misleading as it might be possible to resolve small scale structures while large scale structures are poorly resolved.

We advocate for the use of spatial resolution and model variance to better understand the inherent properties of inverse problems. Spatial resolution is especially compelling as it does not require experimental data and can therefore play an important role when designing the inverse problem. We compared the spatial resolution of two models in Figure 8 and saw improvements when a single ground magnetometer was included. Figure 10 shows how many ground magnetometers will be in EZIE's field of view as a function of quasi-dipole longitude (Laundal & Richmond, 2017), in the northern hemisphere. Figure 10 is based on the ground magnetometers available from SuperMag (https://supermag.jhuapl.edu/). This assumes that the distance between the blue and red track is 1,000 km, the orbit is north/south and measurements are taken between 60° and 75° latitude. Based on the median of the distribution there will typically be around seven ground magnetometers in EZIE's field of view. Therefore, it seems natural to include ground magnetometers as they can provide valuable information. Likewise, the measurements by EZIE fit neatly into the SECS-based Lompe technique (Hovland et al., 2022; Laundal et al., 2022), that like AMIE Richmond and Kamide (1988) and AMGeO Collaboration (2019) combines multiple types of measurements to model the ionospheric electric field.

In this study ground magnetometer measurements were included to illustrate the value of using spatial resolution and model variance to compare and assess the performance of models. It is outside the scope of this study to analyze the implications of including multiple ground magnetometer stations. However, in a future study it would be interesting to carry out case studies for when the EZIE orbit intersects with certain ground magnetometer arrays, for example, North America, Greenland, and Fennoscandia.

Spatial resolution, model variance and regularization are related. The smallest spatial scale a model can resolve increases when the regularization is increased. It is therefore clear that the choice of regularization parameter is important. Figure 4 shows how the $\lambda$-relation is determined. The question is; what range of $\lambda_1$ and $\lambda_2$ should be tested? It can be a good idea to scale $\lambda_1$ by some quantity of $\boldsymbol{G}^T\boldsymbol{C}_d^{-1}\boldsymbol{G}$, for example, median of the diagonal,

such that $\lambda_1 = 1$ will have a significant impact. By scaling $\lambda_1$ in this way, we are almost certain to find the desired trade-off with $\lambda_1 \in [10^{-3}; 10^{3}]$. Unfortunately, determining a range for $\lambda_2$ is not as straightforward. It can be scaled in a similar fashion as $\lambda_1$, but since it controls gradient smoothing its magnitude does not have to be close to 1. The example shown here is well-behaved, such that the surface formed by $\lambda_1$, $\lambda_2$ and the Hoyer index has one clear maximum before the model solution becomes dominated by zonal structures. For this reason, it has not been necessary to define an upper threshold for $\lambda_2$. However, this can become relevant if the measurement geometry changes. The measurement geometry is not only determined by the viewing angle of the instruments, but also by where the measurements lie on the spherical surface and the declination of the tracks. Changing these aspects of the measurement geometry determines if $\lambda_2$, controlling east/west gradient smoothing, smooths structures cross-track direction, along-track direction or some direction in between. In addition, it is possible for the gradient smoothing to essentially loop around on itself, at higher latitudes. This is observed as an additional peak in the Hoyer index at large $\lambda_2$ values. By examining the PSF and/or model solution for this last peak it is easily concluded that it is undesirable. We therefore suggest that the localization error (Oldenborger & Routh, 2009) can be used to indicate the upper limit of $\lambda_2$. The localization error is determined by evaluating the Euclidean distance between the maximum of the $\delta$-function and the PSF. Ideally, the two maxima should be at the same location. However, small deviations are likely to occur. By examining the localization error we found that a discontinuous increase occurs at large $\lambda_2$ values and the $\lambda_2$ at which it happens increases with $\lambda_1$. By locating the discontinuity a threshold after which $\lambda_2$ should not be increased further can be determined.

The $\lambda$-relation is defined based on how the AF of a specific model parameter behaves. If we chose another model parameter the relation would change. However, the geometry between the green and red track of Figure 4 is symmetric, and changing to a neighboring model parameter in the along-track direction would not lead to any significant change. This is not the case near the end of the data tracks. At the top of the red track, it is easy to find a measurement that does not have a counterpart on the green track if a path of equal latitude is followed. This is an issue because we have imposed prior information about how the structures are aligned (east/west) and thus with sufficient east/west gradient smoothing model parameters on such a path are subject to extrapolation and not interpolation. Therefore, it is wise to avoid determining the $\lambda$-relation based on model parameters that are not constrained by data on either side when $\lambda_2$ is increased.

The presented method for combining regularization parameters works well for the measurement geometry of EZIE. However, there are alternatives to tackling multiple regularization parameters. Belge et al. (2002) developed a method for creating an L-hypersurface allowing for the determination of any number of regularization parameters. Working in multiple dimensions tends to be computationally expensive and it can therefore be advantageous to try and reduce the dimensionality by using the $\lambda$-relation. It is also possible to consider these regularization parameters as model parameters and embrace the non-linearity of the problem. If so, a solution can be found using Monte-Carlo Markov-Chain algorithms. In these types of algorithms the posterior model distribution is explored by continuously solving the forward problem. However, with a large number of model parameters comes the curse of dimensionality which can make these algorithms impractical. It is especially difficult if the posterior model covariance turns out to be multi-modal. Alternatively, *model selection* (Akaike, 1974; Virtanen et al., 2018) can be used to determine an adequate level of model complexity. Here the grid resolution could be varied while calculating the likelihood of the associated solution, for example, using the Akaike Information Criterion or the Bayesian Information Criterion (Akaike, 1974; Burnham & Anderson, 2002). The solution that reproduces the observations best while keeping the model complexity low can then be selected. This could also be done with anisotropic grids to accommodate variations in data coverage and/or quality. Instead of using an anisotropic grid it is also possible to use spatially varying regularization parameters such that local variations of a regularization parameter does not affect the solution globally (Roininen et al., 2014). The approach for determining the $\lambda$-relation (Figure 4) was initially carried out for all cross-track locations to determine position dependent east/west smoothing. However, this was found to cause multi modality of the PSFs and thereby affect the spatial resolution estimation and was therefore not used.

The EZIE satellites will measure 118 GHz oxygen emission using the Microwave Electrojet Magnetogram (Yee et al., 2021). In the mesosphere, the foot point will be a few tens of km, but vary with viewing angle and the altitude of the satellite. Spatial scales small enough to vary within the MEM's field of view could lead to a higher measurement uncertainty. The MHD, shown in Figure 1, contain large-scale features. In the scenario where parts of the measurement track is co-located with structures small enough to affect measurement uncertainty the spatial resolution of the surrounding area could be affected.

## 6. Conclusion

In this study we have presented a method for quantifying spatial resolution, and illustrated this via an example in which the SECS technique (Amm et al., 2002) was employed to model the equivalent ionospheric current using synthetic measurements from one of the EZIE satellites (Laundal et al., 2021; Yee et al., 2021). The spatial resolution is found to be around 200–400 km in the cross-track direction and around 100–300 km in the along-track direction. This is sufficient to resolve mesoscale features (100–500 km), which is necessary to answer the science questions posed by the EZIE mission. In addition, we have compared the spatial resolution and model variance to another model which includes a single ground magnetometer. This comparison shows that the cross-track spatial resolution around the ground magnetometer improves. However, the comparison also illustrated that there are limitations to how small spatial scales the ground magnetometer can resolve. This is due to the ∼80 km distance between the peak 118 GHz thermal oxygen emission and the ground location. Comparison of the posterior data covariance of the two models shows how inclusion of the ground magnetometer reduces the variance locally and globally. We attribute this to a significantly lower uncertainty associated with the ground magnetometer measurements, thus providing a better constraint for the magnitude of the model parameters. We hope that by further developing the concept of spatial resolution to the ionospheric science community we improve the way that we analyze and draw conclusions based on inverse models.

Besides the quantification of spatial resolution and comparison of models, we have presented a method for combining two regularization parameters based on the model resolution matrix. This makes determining the trade-off between minimizing data misfit and the regularization term easier. Our method enables comparison between the two models, one with and one without a ground magnetometer, as the need to choose the regularization parameters by manual tuning is not needed. In particular, the method is highly efficient in scenarios where measurement geometry remains constant, for example, ground magnetometer arrays, as it does not depend on the actual measurement values, but rather the location and uncertainty of the measurements.

## Data Availability Statement

The simulation dataset used in this study is available at Zenodo via https://doi.org/10.5281/zenodo.7823088 (Madelaire, 2023).

**Acknowledgments**
This work was funded by the Research Council of Norway (RCN) under Contract 223252/F50. KL and JR were also funded by the RCN under Contract 300844/F50. KL and SH were also funded by the Trond Mohn Foundation.

## References

Akaike, H. (1974). A new look at the statistical model identification. *IEEE Transactions on Automatic Control*, *19*(6), 716–723. https://doi.org/10.1109/TAC.1974.1100705

AMGeO Collaboration. (2019). A collaborative data science platform for the geospace community: Assimilative mapping of geospace observations (AMGeO) v1.0.0. *Zenodo*. https://doi.org/10.5281/zenodo.3564914

Amm, O., Engebretson, M. J., Hughes, T., Newitt, L., Viljanen, A., & Watermann, J. (2002). A traveling convection vortex event study: Instantaneous ionospheric equivalent currents, estimation of field-aligned currents, and the role of induced currents. *Journal of Geophysical Research*, *107*(A11), SIA1-1–SIA1-11. https://doi.org/10.1029/2002JA009472

Amm, O., Opgenoorth, H., & Viljanen, A. (2010). Ground-based magnetometer arrays in space research: A brief review. In *Egu general assembly conference abstracts* (p. 4889).

Amm, O., & Viljanen, A. (1999). Ionospheric disturbance magnetic field continuation from the ground to the ionosphere using spherical elementary current systems. *Earth Planets and Space*, *51*(6), 431–440. https://doi.org/10.1186/BF03352247

An, M. (2012). A simple method for determining the spatial resolution of a general inverse problem. *Geophysical Journal International*, *191*(2), 849–864. https://doi.org/10.1111/j.1365-246X.2012.05661.x

Arvai, K. (2020). kneed. *Zenodo*. https://doi.org/10.5281/zenodo.6496267

Aster, R. C., Borchers, B., & Thurber, C. H. (2013). Chapter four - Tikhonov regularization. In R. C. Aster, B. Borchers, & C. H. Thurber (Eds.), *Parameter estimation and inverse problems* (2nd ed.), (pp. 93–127). Academic Press. https://doi.org/10.1016/B978-0-12-385048-5.00004-5

Barmin, M. P., Ritzwoller, M. H., & Levshin, A. L. (2001). A fast and reliable method for surface wave tomography. *Pure and Applied Geophysics*, *158*(8), 1351–1375. https://doi.org/10.1007/PL00001225

Bauer, F., & Lukas, M. A. (2011). Comparing parameter choice methods for regularization of ill-posed problems. *Mathematics and Computers in Simulation*, *81*(9), 1795–1841. https://doi.org/10.1016/j.matcom.2011.01.016

Belge, M., Kilmer, M. E., & Miller, E. L. (2002). Efficient determination of multiple regularization parameters in a generalized L-curve framework. *Inverse Problems*, *18*(4), 1161–1183. https://doi.org/10.1088/0266-5611/18/4/314

Burnham, K. P., & Anderson, D. R. (2002). *Model selection and multimodel inference*. Springer. https://doi.org/10.1007/b97636

Chiao, L.-Y., Chen, Y.-N., & Gung, Y. (2014). Constructing empirical resolution diagnostics for kriging and minimum curvature gridding. *Journal of Geophysical Research: Solid Earth*, *119*(5), 3939–3954. https://doi.org/10.1002/2013JB010364

Cousins, E. D. P., Matsuo, T., & Richmond, A. D. (2015). Mapping high-latitude ionospheric electrodynamics with superdarn and ampere. *Journal of Geophysical Research: Space Physics*, *120*(7), 5854–5870. https://doi.org/10.1002/2014JA020463

Friis-Christensen, E., McHenry, M. A., Clauer, C. R., & Vennerstrøm, S. (1988). Ionospheric traveling convection vortices observed near the polar cleft: A triggered response to sudden changes in the solar wind. *Geophysical Research Letters*, *15*(3), 253–256. https://doi.org/10.1029/GL015i003p00253

Gustavsson, B. (1998). Tomographic inversion for ALIS noise and resolution. *Journal of Geophysical Research*, *103*(A11), 26621–26632. https://doi.org/10.1029/98JA00678

Hansen, P. C. (1992). Analysis of discrete ill-posed problems by means of the L-curve. *SIAM Review*, *34*(4), 561–580. https://doi.org/10.1137/1034115

Hansen, P. C., Jensen, T. K., & Rodriguez, G. (2007). An adaptive pruning algorithm for the discrete L-curve criterion. *Journal of Computational and Applied Mathematics*, *198*(2), 483–492. https://doi.org/10.1016/j.cam.2005.09.026

Hovland, A. Ø., Laundal, K. M., Reistad, J. P., Hatch, S. M., Walker, S. J., Madelaire, M., & Ohma, A. (2022). The Lompe code: A python toolbox for ionospheric data analysis. *Frontiers in Astronomy and Space Sciences*, *9*, 1025823. https://doi.org/10.3389/fspas.2022.1025823

Hoyer, P. O. (2004). Non-negative matrix factorization with sparseness constraints. *Journal of Machine Learning Research*, *5*, 1457–1469.

Hurley, N. P., & Rickard, S. T. (2008). Comparing measures of sparsity. arXiv. https://doi.org/10.48550/ARXIV.0811.4706

Juusola, L., Vanhamäki, H., Viljanen, A., & Smirnov, M. (2020). Induced currents due to 3D ground conductivity play a major role in the interpretation of geomagnetic variations. *Annales Geophysicae*, *38*(5), 983–998. https://doi.org/10.5194/angeo-38-983-2020

Laundal, K. M., Reistad, J. P., Hatch, S. M., Madelaire, M., Walker, S., Hovland, A., et al. (2022). Local mapping of polar ionospheric electrodynamics. *Journal of Geophysical Research: Space Physics*, *127*(5), e2022JA030356. https://doi.org/10.1029/2022JA030356

Laundal, K. M., & Richmond, A. (2017). Magnetic coordinate systems. *Space Science Reviews*, *206*(1–4), 27–59. https://doi.org/10.1007/s11214-016-0275-y

Laundal, K. M., Yee, J. H., Merkin, V. G., Gjerloev, J. W., Vanhamäki, H., Reistad, J. P., et al. (2021). Electrojet estimates from mesospheric magnetic field measurements. *Journal of Geophysical Research: Space Physics*, *126*(5), e2020JA028644. https://doi.org/10.1029/2020JA028644

Lévěque, J.-J., Rivera, L., & Wittlinger, G. (1993). On the use of the checker-board test to assess the resolution of tomographic inversions. *Geophysical Journal International*, *115*(1), 313–318. https://doi.org/10.1111/j.1365-246X.1993.tb05605.x

Madelaire, M. (2023). Replication data for "spatial resolution in inverse problems: The EZIE satellite mission" [Dataset]. Zenodo. https://doi.org/10.5281/zenodo.7823088

Madelaire, M., Laundal, K. M., Reistad, J. P., Hatch, S. M., & Ohma, A. (2022). Transient high latitude geomagnetic response to rapid increases in solar wind dynamic pressure. *Frontiers in Astronomy and Space Sciences*, *9*, 953954. https://doi.org/10.3389/fspas.2022.953954

Matsuo, T., Knipp, D. J., Richmond, A. D., Kilcommons, L., & Anderson, B. J. (2015). Inverse procedure for high-latitude ionospheric electrodynamics: Analysis of satellite-borne magnetometer data. *Journal of Geophysical Research: Space Physics*, *120*(6), 5241–5251. https://doi.org/10.1002/2014JA020565

Merkin, V. G., & Lyon, J. G. (2010). Effects of the low-latitude ionospheric boundary condition on the global magnetosphere. *Journal of Geophysical Research*, *115*(A10), A10202. https://doi.org/10.1029/2010JA015461

Miller, C. R., & Routh, P. S. (2007). Resolution analysis of geophysical images: Comparison between point spread function and region of data influence measures. *Geophysical Prospecting*, *55*(6), 835–852. https://doi.org/10.1111/j.1365-2478.2007.00640.x

Neumaier, A. (1998). Solving ill-conditioned and singular linear systems: A tutorial on regularization. *SIAM Review*, *40*(3), 636–666. https://doi.org/10.1137/S0036144597321909

Oldenborger, G. A., & Routh, P. S. (2009). The point-spread function measure of resolution for the 3-D electrical resistivity experiment. *Geophysical Journal International*, *176*(2), 405–414. https://doi.org/10.1111/j.1365-246X.2008.04003.x

Pascual-Marqui, R. D. (1999). Review of methods for solving the EEG inverse problem.

Rawlinson, N., & Spakman, W. (2016). On the use of sensitivity tests in seismic tomography. *Geophysical Journal International*, *205*(2), 1221–1243. https://doi.org/10.1093/gji/ggw084

Ren, Z., & Kalscheuer, T. (2020). Uncertainty and resolution analysis of 2D and 3D inversion models computed from geophysical electromagnetic data. *Surveys in Geophysics*, *41*(1), 47–112. https://doi.org/10.1007/s10712-019-09567-3

Richmond, A. D., & Kamide, Y. (1988). Mapping electrodynamic features of the high-latitude ionosphere from localized observations: Technique. *Journal of Geophysical Research*, *93*(A6), 5741–5759. https://doi.org/10.1029/JA093iA06p05741

Roininen, L., Huttunen, J., & Lasanen, S. (2014). Whittle-Matérn priors for Bayesian statistical inversion with applications in electrical impedance tomography. *Inverse Problems and Imaging*, *8*(2), 561–586. https://doi.org/10.3934/ipi.2014.8.561

Satopaa, V., Albrecht, J., Irwin, D., & Raghavan, B. (2011). Finding a "kneedle" in a haystack: Detecting knee points in system behavior. In *2011 31st international conference on distributed computing systems workshops* (pp. 166–171). https://doi.org/10.1109/ICDCSW.2011.20

Sorathia, K. A., Merkin, V. G., Panov, E. V., Zhang, B., Lyon, J. G., Garretson, J., et al. (2020). Ballooning-interchange instability in the near-Earth plasma sheet and auroral beads: Global magnetospheric modeling at the limit of the MHD approximation. *Geophysical Research Letters*, *47*(14), e2020GL088227. https://doi.org/10.1029/2020GL088227

Tarantola, A., & Valette, B. (1982). Inverse problems = quest for information. *Journal of Geophysics*, *50*, 159–170.

Tikhonov, A. N., & Arsenin, V. Y. (1977). *Solutions of ill-posed problems*. John Wiley & Sons, V. H. Winston & Sons. (Translated from the Russian, Preface by translation editor Fritz John, Scripta Series in Mathematics).

Virtanen, I. I., Gustavsson, B., Aikio, A., Kero, A., Asamura, K., & Ogawa, Y. (2018). Electron energy spectrum and auroral power estimation from incoherent scatter radar measurements. *Journal of Geophysical Research: Space Physics*, *123*(8), 6865–6887. https://doi.org/10.1029/2018JA025636

Yee, J. H., Gjerloev, J., & Wu, D. (2021). Remote sensing of magnetic fields induced by electrojets from space. In *Upper atmosphere dynamics and energetics* (pp. 451–468). American Geophysical Union (AGU). https://doi.org/10.1002/9781119815631.ch21

Yee, J. H., Gjerloev, J., Wu, D., & Schwartz, M. J. (2017). First application of the Zeeman technique to remotely measure auroral electrojet intensity from space. *Geophysical Research Letters*, *44*(20), 10134–10139. https://doi.org/10.1002/2017GL074909

Zhang, B., Sorathia, K. A., Lyon, J. G., Merkin, V. G., Garretson, J. S., & Wiltberger, M. (2019). Gamera: A three-dimensional finite-volume MHD solver for non-orthogonal curvilinear geometries. *The Astrophysical Journal - Supplement Series*, *244*(1), 20. https://doi.org/10.3847/1538-4365/ab3a4c